

LOCALLY SUBSPACE-INFORMED NEURAL OPERATORS FOR EFFICIENT MULTISCALE PDE SOLVING

Alexander Rudikov
XXXX,
Institute of Numerical Mathematics
ay.rudikov@gmail.com

Vladimir Fanaskov
XXXX, Applied AI Institute

Sergei Stepanov
North-Eastern Federal University

Buzheng Shan
Department of Mathematics,
Texas A&M University

Ekaterina Muravleva
Institute of Numerical Mathematics

Yalchin Efendiev
Department of Mathematics,
Texas A&M University

Ivan Oseledets
XXXX,
Institute of Numerical Mathematics

ABSTRACT

We propose GMsFEM-NO, a novel hybrid framework that combines the robustness of the Generalized Multiscale Finite Element Method (GMsFEM) with the computational speed of neural operators (NOs) to create an efficient method for solving heterogeneous partial differential equations (PDEs). GMsFEM builds localized spectral basis functions on coarse grids, allowing it to capture important multiscale features and solve PDEs accurately with less computational effort. However, computing these basis functions is costly. While NOs offer a fast alternative by learning the solution operator directly from data, they can lack robustness. Our approach trains a NO to instantly predict the GMsFEM basis by using a novel subspace-informed loss that learns the entire relevant subspace, not just individual functions. This strategy significantly accelerates the costly offline stage of GMsFEM while retaining its foundation in rigorous numerical analysis, resulting in a solution that is both fast and reliable. On standard multiscale benchmarks—including a linear elliptic diffusion problem and the nonlinear, steady-state Richards equation—our GMsFEM-NO method achieves a reduction in solution error compared to standalone NOs and other hybrid methods. The framework demonstrates effective performance for both 2D and 3D problems. A key advantage is its discretization flexibility: the NO can be trained on a small computational grid and evaluated on a larger one with minimal loss of accuracy, ensuring easy scalability. Furthermore, the resulting solver remains independent of forcing terms, preserving the generalization capabilities of the original GMsFEM approach. Our results prove that combining NO with GMsFEM creates a powerful new type of solver that is both fast and accurate.

1 INTRODUCTION

Many practical multiscale problems involve highly heterogeneous properties with high-contrast variations across multiple scales, posing significant challenges for the numerical solution of partial differential equations (PDEs). A well-established approach for such problems is the Generalized Multiscale Finite Element Method (GMsFEM) Efendiev et al. (2011; 2013); Chung et al. (2016),

which constructs localized spectral basis functions on coarse grids. By solving local eigenproblems, GMsFEM captures fine-scale information, enabling accurate coarse-scale solutions. However, this accuracy comes at a high computational cost due to the expense of solving these local eigenproblems.

Recently, data-driven solvers, particularly neural operators (NOs) like Fourier Neural Operators (FNOs) Li et al. (2020); Kovachki et al. (2023); Fanaskov & Oseledets (2023); Tran et al. (2021) and DeepONets Lu et al. (2021); Wang et al. (2021), have emerged as a powerful alternative for accelerating PDE simulations Azizzadenesheli et al. (2024); Karniadakis et al. (2021). While effective for problems with smooth coefficients, standard NOs often struggle to efficiently capture the localized features of high-contrast heterogeneities, typically requiring extensive data and large network architectures.

In this work, we introduce GMsFEM-NO, a hybrid framework that combines the robustness of GMsFEM with the speed of neural operators. Our key innovation is a subspace-informed NO that learns to map a heterogeneous coefficient field directly to the low-dimensional subspace spanned by the GMsFEM basis functions. Instead of learning individual basis functions—which can be sensitive to small perturbations—we design a novel subspace-aware loss function that enforces physical consistency at the subspace level. This approach offers several advantages: it is more data-efficient than learning the full PDE solution, as the basis functions are smoother and of lower dimension; and it is more robust than a pure NO, as the final solution is obtained through a GMsFEM, ensuring legitimacy even with imperfect basis predictions.

Our approach is distinct from existing hybrid methods Bhattacharya et al. (2024); Vasilyeva et al. (2020); Wang et al. (2020); Liu et al. (2023); Kröpfl et al. (2022; 2025) that combine machine learning with numerical homogenization/upscaling/macroscopic-modeling. Those methods typically assume a known macroscopic equation form and learn effective coefficients, which is infeasible for problems without scale separation and with high contrast. In contrast, GMsFEM-NO learns the macroscopic solution space itself, in the form of multiscale basis functions, making it suitable for these more challenging settings. A related approach Spiridonov et al. (2025) used a fully connected neural network to predict an additional basis function for the steady-state Richards equation Richards (1931); Farthing & Ogden (2017), supplementing an existing set of precomputed basis functions. While this approach enhanced prediction accuracy, it failed to deliver computational efficiency gains because traditional methods still generated most basis functions. Furthermore, the simplicity of the fully connected architecture limited its ability to account for spatial variations, potentially compromising prediction accuracy for high-contrast data. Another category of related work aims to reduce the computational cost of PDE solving via reduced-order modeling (POD Volkwein (2013), DeepPOD Franco et al., and PCANet Bhattacharya et al. (2021)). DeepPOD and PCANet also leverage neural networks to learn compact solution representations, providing a relevant baseline for comparing the efficiency of our method.

We validate GMsFEM-NO on two challenging benchmarks with high-contrast coefficients: a linear elliptic diffusion problem and the nonlinear steady-state Richards equation. Results showed that our approach is better than NO in terms of solution accuracy and requires less training data to achieve similar accuracy. Additionally, it reduces basis-construction time by more than 60 times compared to traditional GMsFEM.

Our main contributions are:

1. We introduce a novel hybrid approach (GMsFEM-NO) that combines the strengths of NOs with GMsFEM (see Fig. 1).
2. A new subspace-informed loss function for learning stable and generalizable solution subspaces.
3. The approach is evaluated on high-contrast PDEs and shown to deliver the same results as GMsFEM at a fraction of the computational cost.
4. Demonstration of resolution invariance of GMsFEM-NO: effective training on low-resolution data for application to high-resolution problems.
5. Superior in-distribution and out-of-distribution performance compared to standard NOs, without requiring domain adaptation.

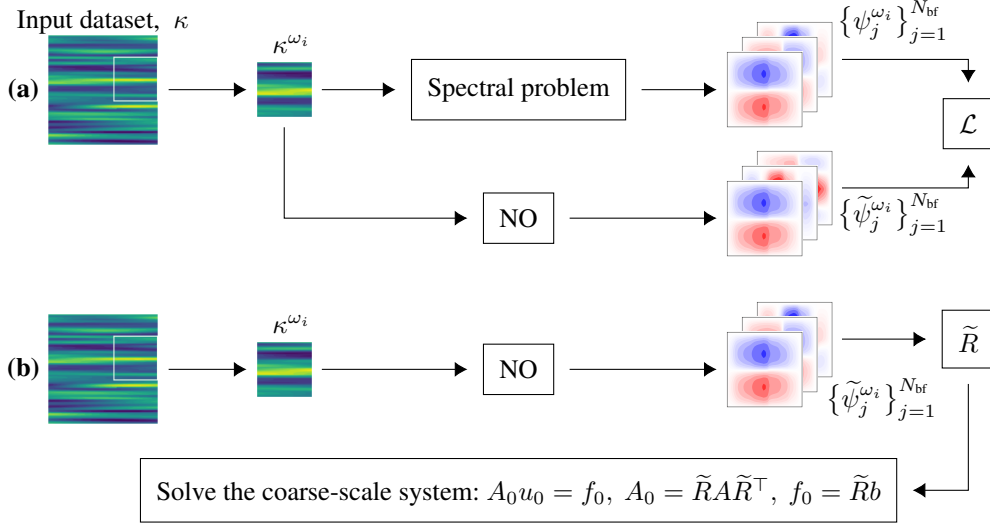


Figure 1: Illustration of training **(a)** and inference **(b)** stages of the proposed GMsFEM-NO method. NO is trained on heterogeneous fields κ^{ω_i} that defined on subdomain ω_i to predict subspace of basis functions $\{\psi_j^{\omega_i}\}_{j=1}^{N_{\text{bf}}}$, where N_{bf} is the number of basis functions. During training the subspace-informed loss \mathcal{L} is applied to align predicted subspace $\{\tilde{\psi}_j^{\omega_i}\}_{j=1}^{N_{\text{bf}}}$ with $\{\psi_j^{\omega_i}\}_{j=1}^{N_{\text{bf}}}$. During inference stage **(b)**, the predicted subspace forms the matrix \tilde{R} that projects matrix A and vectors to the coarse space.

2 LOCALLY SUBSPACE-INFORMED NEURAL OPERATORS

2.1 DIFFUSION EQUATION

We consider the diffusion equation with heterogeneous coefficient

$$-\nabla \cdot (\kappa(x) \nabla u(x)) = f(x), \quad x \in \Omega \equiv (0, 1)^D, \quad u(x)|_{x \in \partial\Omega} = 0, \quad (1)$$

where $\partial\Omega$ is a boundary of the unit hypercube Ω , and $\kappa(x)$ is a heterogeneous field with high contrast. In particular, we assume that $\kappa(x) \geq \varepsilon > 0$, while $\kappa(x)$ can have very large variations. For example, in this work we use $\kappa(x)$ with values in range $[1, 9600]$.

2.2 STEADY-STATE RICHARDS' EQUATION

The steady-state version of Richards' equation, which describes water movement in unsaturated porous media, takes the following form:

$$-\nabla \cdot (\kappa(x, u(x)) \nabla u(x)) = f(x), \quad x \in \Omega \equiv (0, 1)^D, \quad u(x)|_{x \in \partial\Omega} = 0, \quad (2)$$

where $\kappa(x, u(x))$ is unsaturated hydraulic conductivity, $u(x)$ is the water pressure and $f(x)$ is a source or sink term.

We consider the Haverkamp model Haverkamp et al. (1977) to define $\kappa(x, u(x))$:

$$\kappa(x, u(x)) = K_s(x) K_r(u(x)) = \kappa(x) \frac{1}{1 + |u|},$$

where $\kappa(x)$ is a heterogeneous field with high contrast that denotes the permeability of soils, $K_r(u)$ represents the relative hydraulic conductivity, $K_s(x)$ stands for the saturated hydraulic conductivity. All the multiscale heterogeneity is incorporated in $\kappa(x)$ without regard to u , and $\frac{1}{1 + |u|}$ includes all the non-linearity.

2.3 GENERALIZED MULTISCALE FINITE ELEMENT METHOD

2.3.1 MULTISCALE SPACE APPROXIMATION

Multiscale methods Efendiev & Hou (2009) form a broad class of numerical techniques. They are based on constructing multiscale basis functions in local domains to capture fine-scale behavior.

Let \mathcal{T}_H be a coarse mesh of the domain $\Omega \subset \mathbb{R}^D$ (with $D = 2$ or 3), such that $\mathcal{T}_H = \bigcup_{i=1}^{N_c} K_i$, where each K_i is a coarse cell and N_c is the number of coarse cells. Let \mathcal{T}_h be a fine grid obtained by a refinement of \mathcal{T}_H , with $h \ll H$. We denote by $\{x_i\}_{i=1}^{N_v}$ the nodes of the coarse mesh \mathcal{T}_H , where N_v is the number of nodes of the coarse mesh. Let ω_i be the subdomain defined as the collection of coarse cells containing the coarse grid node x_i (see Fig. 2 in Appendix A):

$$\omega_i = \bigcup_j \{K_j \in \mathcal{T}_H : x_i \in \overline{K_j}\}.$$

To ensure accurate approximations on the coarse mesh \mathcal{T}_H , we construct spectral multiscale basis functions following the GMsFEM. GMsFEM contains two stages:

Offline stage:

1. **Coarse and Local Domain Definition:** Define the coarse grid \mathcal{T}_H and generate the associated local domains ω_i for $i = 1, \dots, N_v$.
2. **Local Spectral Problem Solving:** In each local domain ω_i , solve a local spectral problem to obtain a set of eigenvectors $\{\phi_j^{\omega_i}\}_{j=1}^N$, where N is the number of coarse eigenvectors.
3. **Multiscale Basis Function Construction:** Select the first N_{bf} eigenvectors from each ω_i and multiply them by a partition of unity function χ_i Babuska & Lipton (2011); Babuška et al. (2008); Strouboulis et al. (2000) to create the final multiscale basis functions $\{\psi_j^{\omega_i}\}_{j=1}^{N_{\text{bf}}}$, where $N_{\text{bf}} \leq N$.
4. **Global System Assembly:** Map the local degrees of freedom to global and form a restriction matrix R .

Online stage:

1. **Projection:** Use R to project the fine-scale system onto the coarse space.
2. **Solution:** Compute the solution within the coarse multiscale space.
3. **Reconstruction:** Obtain the fine-scale approximation by applying the prolongation operator R^\top to the coarse-scale solution.

2.3.2 SPECTRAL PROBLEM

We denote by $V^h(\Omega)$ the usual finite element discretization of piecewise linear continuous functions with respect to the fine grid \mathcal{T}_h . For each local domain ω_i , we define the **Neumann** matrix $A_h^{\omega_i}$ by

$$v_h^\top A_h^{\omega_i} w_h = \int_{\omega_i} \kappa(x) \nabla v_h \cdot \nabla w_h \, dx, \quad \forall v_h, w_h \in V^h(\omega_i)$$

and the **Mass** matrix $S_h^{\omega_i}$ by

$$v_h^\top S_h^{\omega_i} w_h = \int_{\omega_i} \kappa(x) v_h w_h \, dx, \quad \forall v_h, w_h \in V^h(\omega_i).$$

We consider the finite dimensional symmetric eigenvalue problem

$$A_h^{\omega_i} \phi = \lambda S_h^{\omega_i} \phi$$

and denote its eigenvalues and eigenvectors by $\{\lambda_j^{\omega_i}\}_{j=1}^N$ and $\{\phi_j^{\omega_i}\}_{j=1}^N$, respectively. Note that $\lambda_1^{\omega_i} = 0$ corresponds to the constant eigenvector $\phi_1^{\omega_i} = \text{const}$. We order eigenvalues as

$$\lambda_1^{\omega_i} \leq \lambda_2^{\omega_i} \leq \dots \leq \lambda_j^{\omega_i} \leq \dots$$

The eigenvectors $\{\phi_j^{\omega_i}\}_{j=1}^N$ form an $S_h^{\omega_i}$ -orthonormal basis of $V^h(\omega_i)$.

2.3.3 SOLVING OF THE COARSE-SCALE SYSTEM

For each local domain ω_i , we select eigenvectors corresponding to the $N_{\text{bf}} \leq N$ smallest eigenvalues and define a multiscale subspace

$$\text{span}\{\psi_j^{\omega_i} = \chi_i \phi_j^{\omega_i} \mid j = 1, \dots, N_{\text{bf}}, i = 1, \dots, N_v\} \quad (3)$$

and define the restriction matrix $R^\top = [\psi_1^{\omega_1}, \dots, \psi_{N_{\text{bf}}}^{\omega_1}, \dots, \psi_1^{\omega_{N_v}}, \dots, \psi_{N_{\text{bf}}}^{\omega_{N_v}}]$. Coarse-grid solution is the finite element projection of the fine-scale solution into the space (3). More precisely, multiscale solution u_0 is given by

$$A_0 u_0 = f_0,$$

where $A_0 = RAR^\top$ is the projected system matrix, $f_0 = R^\top b$ is projected right-hand side. The reconstructed fine-scale solution is $u = R^\top u_0$.

2.4 NEURAL OPERATOR

Here we consider one type of NO that employs Fourier modes, but there are no restrictions on using other types of NOs. Fourier neural operators (FNOs) are a class of NOs motivated by Fourier spectral methods. Originally, Li et al. (2020) formulate each operator layer as

$$\mathcal{L}^\ell(z^{(\ell)}) = \sigma[W^{(\ell)}z^{(\ell)} + b^{(\ell)} + \mathcal{K}^\ell(z^{(\ell)})], \quad (4)$$

where $W^{(\ell)}z^{(\ell)} + b^{(\ell)}$ is an affine point-wise map,

$$\mathcal{K}^\ell(z^{(\ell)}) = \text{IFFT}(\mathcal{R}^{(\ell)} \cdot \text{FFT}(z))$$

is a kernel integral operator. The Fourier domain weight matrices $\{\mathcal{R}^{(\ell)}\}_{\ell=1}^L$ require $O(LH^2MD)$ parameters, where H is the hidden size, M is the number of the top Fourier modes that are kept, and D is the dimension of the problem.

In Factorised FNO (F-FNO) Tran et al. (2021), the operator layer in (4) is changed

$$\mathcal{L}^\ell(z^{(\ell)}) = z^{(\ell)} + \sigma[W_2^{(\ell)}\sigma(W_1^{(\ell)}\mathcal{K}^\ell(z^{(\ell)}) + b_1^{(\ell)}) + b_2^{(\ell)}],$$

where $\mathcal{K}^\ell(z^{(\ell)}) = \sum_{d \in D} [\text{IFFT}(\mathcal{R}_d^{(\ell)} \cdot \text{FFT}_d(z^{(\ell)}))]$. In this case, the number of parameters is $O(LH^2MD)$. Therefore, the FFNO reduces model complexity and scales efficiently to deeper networks.

2.5 PROPOSED METHOD

2.5.1 GMSFEM-NO ALGORITHM

We propose an efficient hybrid method for generating basis functions in the GMSFEM using NOs, significantly accelerating the offline stage.

Local domains vary in shape and orientation (see Appendix A), where orientation refers to the relative placement of the coarse node x_i shared by all cells in the local domain. We address this variability by categorizing the local domains based on their geometry: into **full**, **half**, and **corner** types in 2D, and into **full**, **half**, **quarter**, and **corner** types in 3D (see Appendix A). Before training, we normalize the orientation of each local domain by rotating both the input data and the target basis functions, ensuring a standardized coarse node x_i position within each group. This preprocessing step guarantees consistency in the input structure for the NO.

We train separate NOs, each specialized for one domain group (see Appendix B). Each NO predicts N_{bf} basis functions for local domains within its assigned category. This group-specific approach improves prediction accuracy by accounting for geometric variations across local domain types.

For test data, we first decompose the computational domain into local domains. The corresponding NO then generates the required basis functions. The predicted basis functions are extended to the domain Ω (with zeros padded outside their respective local domains) and vectorized to construct the

restriction matrix R . Finally, the online stage of GMsFEM is executed to compute the multiscale solution.

This approach substantially reduces offline computational costs while maintaining the accuracy and flexibility of GMsFEM, making it particularly suitable for problems with heterogeneous or highly varying coefficients.

2.5.2 SUBSPACE-INFORMED LOSS FUNCTIONS

The selection of an appropriate loss function is critical when training NOs. We propose a **Subspace Alignment Loss (SAL)** that directly optimizes the geometric consistency of the learned subspaces. Let $R^i = [\psi_1^i, \dots, \psi_{N_{\text{bf}}}^i]^\top$ represent the target subspace basis and \tilde{R}^i denote the predicted subspace. The SAL measures alignment between subspaces using their orthonormalized bases Q_{R^i} and $Q_{\tilde{R}^i}$:

$$\mathcal{L}_{\text{SAL}} = \mathbb{E}_i \left[N_{\text{bf}} - \|Q_{R^i}^\top Q_{\tilde{R}^i}\|_F^2 \right], \quad (5)$$

where the Frobenius norm term $\|Q_{R^i}^\top Q_{\tilde{R}^i}\|_F^2$ quantifies the subspace overlap, achieving its maximum value N_{bf} when subspaces are perfectly aligned. Appendix C proves SAL’s theoretical foundation and provides error bounds connecting subspace alignment to solution accuracy.

While SAL ensures subspace coherence, it may overlook finer discrepancies in how functions are projected onto the subspaces. To enforce consistency in projection behavior, we introduce a **Projection Regularization** term. This term evaluates the discrepancy between projections of a randomized test vector v^i onto the target and predicted subspaces, governed by their projection matrices P_{R^i} and $P_{\tilde{R}^i}$:

$$\mathcal{L}_{\text{SAL-PR}} = \mathcal{L}_{\text{SAL}} + \lambda \cdot \mathbb{E}_{i,c} \left\| (P_{R^i} - P_{\tilde{R}^i}) v^i \right\|_2^2, \quad c \sim \mathcal{N}(0, I), \quad (6)$$

where $v^i = \sum_{k=1}^{N_{\text{bf}}} c_k \psi_k^i$, $P_{R^i} = Q_{R^i} Q_{R^i}^\top$, $P_{\tilde{R}^i} = Q_{\tilde{R}^i} Q_{\tilde{R}^i}^\top$, and λ is a hyperparameter.

We compare proposed loss functions (5), (6) with conventional one which is L_2 loss. Since basis functions are defined only up to their sign (see Appendix E), the conventional L_2 loss is adapted to account for this invariance, resulting in the Relative Basis Function L_2 Loss (RBFL₂):

$$\mathcal{L}_{\text{RBFL}_2} = \mathbb{E}_{i,j} \left[\min \left(\frac{\|\psi_j^i - \tilde{\psi}_j^i\|_2^2}{\|\psi_j^i\|_2^2}, \frac{\|\psi_j^i + \tilde{\psi}_j^i\|_2^2}{\|\psi_j^i\|_2^2} \right) \right], \quad (7)$$

where ψ_j^i and $\tilde{\psi}_j^i$ denote the j -th target and predicted basis functions for the i -th local domain ω_i . The minimization over $\pm \tilde{\psi}_j^i$ ensures invariance to sign permutations.

3 RESULTS

We use datasets of 2D coefficients at resolutions of 100^2 and 250^2 , and 3D coefficients at 50^3 and 100^3 (see example in Appendix F). The domain is partitioned into N_v subdomains corresponding to coarse grids (e.g., $N_v = 36$ for 5×5 , 121 for 10×10 , 216 for $5 \times 5 \times 5$, 729 for $8 \times 8 \times 8$). For all grid sizes except $100 \times 100 \times 100$, we used 1000 samples (800 train, 200 test). For the $100 \times 100 \times 100$ grid, we used 150 train and 50 test samples due to computational constraints. The different local domain types occur with varying frequencies within a single sample (see Appendix B). For training NOs, we utilize the first 8 basis functions (N_{bf}) per subdomain as training targets.

To evaluate method robustness, we consider two right-hand side configurations:

- Uniform unit forcing term

$$f(x) = 1. \quad (8)$$

- Spatially variable forcing (see Appendix F) defined by

$$f(x) \sim \gamma \cdot \mathcal{N} \left(\alpha \cdot (I - \Delta)^{-\beta} \right). \quad (9)$$

To measure quality of the obtained solutions on fine grid, we use the following metrics:

$$L_2 = \mathbb{E}_n \left[\sqrt{\frac{\int_{\Omega} |u_h^n - \tilde{u}_h^n|^2 dx}{\int_{\Omega} |u_h^n|^2 dx}} \right], \quad H_1 = \mathbb{E}_n \left[\sqrt{\frac{\int_{\Omega} |\nabla u_h^n - \nabla \tilde{u}_h^n|^2 dx}{\int_{\Omega} |\nabla u_h^n|^2 dx}} \right].$$

All experiments were performed on a single Nvidia Tesla H100 80Gb HBM3. The comparison of our approach with baseline methods is presented in Appendix G.

3.1 $\mathcal{L}_{\text{RBFL}_2}$ VS. \mathcal{L}_{SAL} , $\mathcal{L}_{\text{SAL-PR}}$

To determine the optimal training configuration for the NOs predicting basis function subspaces, we performed a grid search over architectural parameters and training hyperparameters. Full specifications (except loss function type) are in Appendix H. Loss function results for $N_{\text{bf}} = 8$ are shown in Table 1. For $N_{\text{bf}} = 4$, results are in Appendix J.

As shown in Table 1, $\mathcal{L}_{\text{RBFL}_2}$ underperforms compared to our proposed subspace alignment losses (\mathcal{L}_{SAL} , $\mathcal{L}_{\text{SAL-PR}}$). For the Richards equation with simple right-hand side (8) and $N_{\text{bf}} = 8$, our proposed loss improves the relative L_2 metric by a factor of 1.8. Notably, the projection regularization term in $\mathcal{L}_{\text{SAL-PR}}$ yielded nearly identical results to \mathcal{L}_{SAL} . While projection regularization had a minimal impact on smaller grids—likely because the subspace alignment term alone suffices—its effect became significant for larger problems. For the 250^2 grid using Richards’ equation with right-hand side (8), it reduced the L_2 error from 1.82% to 1.72% (see Table 3).

Table 1: Performance comparison of loss functions for NO training (100×100 grid, $N_v = 36$).

N_{bf}	Dataset	$\mathcal{L}_{\text{RBFL}_2}$		\mathcal{L}_{SAL}		$\mathcal{L}_{\text{SAL-PR}}$	
		L_2	H_1	L_2	H_1	L_2	H_1
8	Diffusion, 8	1.75%	14.83%	1.06%	11.57%	1.06%	11.65%
	Diffusion, 9	3.53%	21.77%	2.82%	19.07%	2.81%	19.03%
	Richards, 8	3.46%	15.04%	1.88%	11.10%	1.87%	11.25%
	Richards, 9	3.77%	22.38%	2.99%	19.61%	2.99%	19.60%

3.2 GMSFEM vs. GMSFEM-NO

In this section, we compare the performance of the original GMSFEM and our proposed GMSFEM-NO methods in terms of solution accuracy (quantified by L_2 and H_1 metrics) and computational efficiency for basis functions generation. For large-scale 3D simulations ($100 \times 100 \times 100$ grid), we employed the GMSFEM-NO method with the SAL loss. Although the SAL-PR loss offers benefits for smaller problems (see Appendix D), its computational cost becomes prohibitive at this scale, making the standard SAL loss the practical choice.

As shown in Tables 2, 3, 4 and 5, GMSFEM-NO achieves nearly identical L_2 and H_1 errors to GMSFEM across all datasets and grid sizes. While GMSFEM-NO shows slightly better results for some configurations, this is likely due to statistical variation. The same behaviour is observed for the time-dependent equation and the diffusion equation with mixed boundary conditions (see Appendix L and M); these experiments were conducted solely on the 250×250 grid.

Table 6 compares the time required to generate 8 basis functions using the GMSFEM offline stage and GMSFEM-NO for different grid sizes and N_v values. GMSFEM-NO employs several NOs, one for each local domain type. The proposed method achieves more than $60\times$ speedup, demonstrating its computational superiority. Basis calculation speedup grows with grid size and dimensionality.

While GMSFEM-NO reduces the cost of the traditional GMSFEM offline stage over many subsequent simulations, it does not eliminate cost of train data generation and training. The breakeven point, defined as the number of inference samples required to offset these initial costs, is derived in the Appendix N.

Table 2: Performance comparison of GMsFEM and GMsFEM-NO for 2D (100×100 , $N_v = 36$).

N_{bf}	Dataset	GMsFEM		GMsFEM-NO	
		L_2	H_1	L_2	H_1
8	Diffusion, 8	1.15%	11.68%	1.06%	11.57%
	Diffusion, 9	2.82%	19.07%	2.81%	19.03%
	Richards, 8	2.03%	11.68%	1.87%	11.25%
	Richards, 9	3.09%	20.20%	2.99%	19.60%

Table 3: Performance comparison of GMsFEM and GMsFEM-NO for 2D (250×250 , $N_v = 121$).

N_{bf}	Dataset	GMsFEM		GMsFEM-NO, \mathcal{L}_{SAL}		GMsFEM-NO, $\mathcal{L}_{\text{SAL-PR}}$	
		L_2	H_1	L_2	H_1	L_2	H_1
8	Diffusion, 8	1.12%	14.01%	1.13%	13.92%	1.05%	14.07%
	Diffusion, 9	1.60%	21.49%	1.62%	22.50%	1.60%	22.03%
	Richards, 8	1.79%	14.57%	1.82%	14.27%	1.72%	14.53%
	Richards, 9	1.62%	21.76%	1.62%	22.62%	1.60%	22.13%

Table 4: Performance comparison of GMsFEM and GMsFEM-NO for 3D ($50 \times 50 \times 50$, $N_v = 216$).

N_{bf}	Dataset	GMsFEM		GMsFEM-NO, \mathcal{L}_{SAL}		GMsFEM-NO, $\mathcal{L}_{\text{SAL-PR}}$	
		L_2	H_1	L_2	H_1	L_2	H_1
8	Diffusion, 8	3.07%	20.72%	3.10%	20.39%	3.10%	20.39%
	Diffusion, 9	5.08%	25.26%	5.01%	24.92%	5.00%	24.86%
	Richards, 8	4.04%	15.43%	4.12%	15.37%	4.14%	15.39%
	Richards, 9	5.02%	24.89%	5.02%	24.92%	5.00%	24.89%

Table 5: Performance comparison of GMsFEM and GMsFEM-NO for 3D ($100 \times 100 \times 100$, $N_v = 729$).

N_{bf}	Dataset	GMsFEM		GMsFEM-NO, \mathcal{L}_{SAL}	
		L_2	H_1	L_2	H_1
8	Diffusion, 8	1.62%	14.76%	1.68%	14.98%
	Diffusion, 9	3.0%	12.55%	3.04%	12.84%
	Richards, 8	2.54%	17.83%	2.57%	17.91%
	Richards, 9	2.55%	17.85%	2.57%	17.91%

Table 6: Basis generation time: GMsFEM-NO vs. standard GMsFEM offline stage.

Grid	N_v	GMsFEM, sec.	GMsFEM-NO, sec.
100×100	36	16.87	0.28
250×250	121	210.5	0.31
$50 \times 50 \times 50$	216	935.4	0.84
$100 \times 100 \times 100$	729	10547.2	1.33

3.3 STANDALONE NOS VS. GMSFEM-NO

In this section, we compare GMSFEM-NO against standalone SOTA NOs, including F-FNO, GNOT Hao et al. (2023) and Transolver++ Luo et al. (2025). While these standalone models offer fast inference, their accuracy deteriorates significantly on high-contrast datasets. As shown in Table 7 (250×250 grid), GMSFEM-NO achieves superior accuracy; for Richards’ equation with a complex source term (9), it reduces the relative L2 error by 2.8× compared to the best standalone NO. Full training details are in Appendix I.

A critical advantage of GMSFEM-NO over the standalone NO lies in its independence from the right-hand side terms of the PDE. The standalone NO exhibits catastrophic failure when tested on out-of-distribution forcing terms, as evidenced in Table 13 in Appendix K.

Since each coefficient contains multiple local domains of each type, GMSFEM-NO requires fewer samples than F-FNO for training. As shown in Table 8, when N_{train} is reduced below 800, the error for F-FNO begins to increase significantly. In contrast, GMSFEM-NO’s accuracy remains stable across the range of 800 to 400 samples. Even with only 200 samples, the performance degradation for GMSFEM-NO remains small; for example, on Richards’ equation with the simple right-hand side (8), the error increases only modestly from 1.85% to 2.07%.

Table 7: Performance comparison of NOs and GMSFEM-NO (250 × 250 grid)

N_{bf}	Dataset	F-FNO	GNOT	Transolver++	GMSFEM-NO
8	Diffusion, 8	1.02%	1.26%	1.15%	1.05%
	Diffusion, 9	4.51%	14.29%	6.63%	1.60%
	Richards, 8	2.44%	2.34%	2.17%	1.72%
	Richards, 9	4.45%	14.69%	8.82%	1.60%

Table 8: Comparison of F-FNO and GMSFEM-NO performance across different training dataset sizes for 250 × 250.

D_{train}		Diffusion, 8	Diffusion, 9	Richards, 8	Richards, 9
200	GMSFEM-NO	1.33%	1.77%	2.07%	1.77%
	F-FNO	2.85%	11.56%	6.52%	11.49%
400	GMSFEM-NO	1.15%	1.63%	1.85%	1.62%
	F-FNO	1.60%	8.16%	4.17%	8.41%
600	GMSFEM-NO	1.12%	1.61%	1.78%	1.61%
	F-FNO	1.21%	4.92%	3.27%	5.43%
800	GMSFEM-NO	1.13%	1.62%	1.82%	1.62%
	F-FNO	1.02%	4.51%	2.44%	4.45%

3.4 GMSFEM-NO FOR DIFFERENT GRIDS

Table 9 demonstrates the resolution invariance of GMSFEM-NO by training the model on a coarse grid and testing it on a finer grid (500 × 500), with results compared against the standard GMSFEM solution computed directly on the fine grid. We used a 10 × 10 coarse grid (121 subdomains) for all experiments. The results demonstrate the stability of the proposed method. GMSFEM-NO performs effectively when evaluated on a grid resolution higher than its training resolution, a key advantage enabled by the neural operator’s ability to generalize to different discretizations.

Table 9: Evaluation of GMsFEM-NO trained on coarse grid and tested on finer grid, with comparison to standard GMsFEM.

		Diffusion, 8	Diffusion, 9	Richards, 8	Richards, 9
Train grid	Test grid	GMsFEM-NO			
100	500	2.42%	2.97%	4.70%	3.49%
250	500	1.45%	1.79%	2.25%	1.97%
		GMsFEM			
	500	1.17%	1.46%	1.93%	1.66%

4 CONCLUSION

In this work, we propose GMsFEM-NO, a novel method for solving multiscale PDEs that employs NOs to predict the multiscale basis function subspaces in the GMsFEM offline stage, replacing the conventional solution of local eigenvalue problems. We validated the method on standard 2D and 3D benchmarks: a linear elliptic diffusion problem and the nonlinear steady-state Richards equation. Additionally, we demonstrated its efficacy for time-dependent equations and problems with mixed boundary conditions in 2D. GMsFEM-NO achieves more than $60\times$ speedup in basis generation compared to standard GMsFEM.

A key contribution is a novel subspace alignment loss function, which enables direct learning of the basis function subspace and improves the L_2 accuracy over conventional $\mathcal{L}_{\text{RBFL}_2}$ loss. The GMsFEM-NO framework remains independent of the PDE’s right-hand side, allowing it to maintain consistent performance across varying forcing terms. This contrasts with standalone NOs, which exhibit errors exceeding 100% on out-of-distribution data. Furthermore, GMsFEM-NO demonstrates greater data efficiency, requiring half the training samples of a comparable NO. A significant advantage is the method’s discretization invariance: GMsFEM-NO performs effectively when evaluated on grid resolutions higher than those used for training, demonstrating strong generalization across different computational meshes. By preserving the mathematical structure of multiscale methods while leveraging NO speed, this work establishes a practical paradigm for heterogeneous PDE simulation.

The primary limitation of our method is its current restriction to structured grids due to the chosen NO architecture. Additionally, our experiments focused on relatively small grid sizes, which may not fully represent large-scale applications. While we successfully tested our approach on time-dependent equations and problems with mixed boundary conditions in 2D, the study was primarily focused on steady-state problems with Dirichlet boundary conditions.

Future work will expand this framework in several key directions. First, we will target more complex PDEs. Second, extending the framework to irregular domains is a critical next step. This is well-supported theoretically, as the GMsFEM methodology is established for unstructured meshes, and can be integrated with geometry-aware NOs like Transolver++. Alongside these goals, we will also investigate performance on finer grid resolutions and the impact of coarse-grid sizing to fully realize the method’s potential for large-scale, real-world simulations.

REFERENCES

- Jørg E Aarnes and Yalchin Efendiev. Mixed multiscale finite element methods for stochastic porous media flows. *SIAM Journal on Scientific Computing*, 30(5):2319–2339, 2008.
- Kamyar Azizzadenesheli, Nikola Kovachki, Zongyi Li, Miguel Liu-Schiaffini, Jean Kossaifi, and Anima Anandkumar. Neural operators for accelerating scientific simulations and design. *Nature Reviews Physics*, 6(5):320–328, 2024.
- Ivo Babuska and Robert Lipton. Optimal local approximation spaces for generalized finite element methods with application to multiscale problems. *Multiscale Modeling & Simulation*, 9(1):373–406, 2011.

- Ivo Babuška, Victor Nistor, and Nicolae Tarfulea. Generalized finite element method for second-order elliptic operators with dirichlet boundary conditions. *Journal of Computational and Applied Mathematics*, 218(1):175–183, 2008.
- Pau Batlle, Matthieu Darcy, Bamdad Hosseini, and Houman Owhadi. Kernel methods are competitive for operator learning. *Journal of Computational Physics*, 496:112549, 2024.
- Thomas Bendokat, Ralf Zimmermann, and P-A Absil. A grassmann manifold handbook: Basic geometry and computational aspects. *Advances in Computational Mathematics*, 50(1):6, 2024.
- Kaushik Bhattacharya, Bamdad Hosseini, Nikola B Kovachki, and Andrew M Stuart. Model reduction and neural networks for parametric pdes. *The SMAI journal of computational mathematics*, 7: 121–157, 2021.
- Kaushik Bhattacharya, Nikola B Kovachki, Aakila Rajan, Andrew M Stuart, and Margaret Trautner. Learning homogenization for elliptic operators. *SIAM Journal on Numerical Analysis*, 62(4): 1844–1873, 2024.
- Xiangning Chen, Chen Liang, Da Huang, Esteban Real, Kaiyuan Wang, Hieu Pham, Xuanyi Dong, Thang Luong, Cho-Jui Hsieh, Yifeng Lu, et al. Symbolic discovery of optimization algorithms. *Advances in neural information processing systems*, 36:49205–49233, 2023.
- Eric T Chung, Yalchin Efendiev, Guanglian Li, and Maria Vasilyeva. Generalized multiscale finite element methods for problems in perforated heterogeneous domains. *Applicable Analysis*, 95(10): 2254–2279, 2016.
- DeepMind, Igor Babuschkin, Kate Baumli, Alison Bell, Surya Bhupatiraju, Jake Bruce, Peter Buchlovsky, David Budden, Trevor Cai, Aidan Clark, Ivo Danihelka, Antoine Dedieu, Claudio Fantacci, Jonathan Godwin, Chris Jones, Ross Hemsley, Tom Hennigan, Matteo Hessel, Shaobo Hou, Steven Kapturowski, Thomas Keck, Iurii Kemaev, Michael King, Markus Kunesch, Lena Martens, Hamza Merzic, Vladimir Mikulik, Tamara Norman, George Papamakarios, John Quan, Roman Ring, Francisco Ruiz, Alvaro Sanchez, Laurent Sartran, Rosalia Schneider, Eren Sezener, Stephen Spencer, Srivatsan Srinivasan, Miloš Stanojević, Wojciech Stokowiec, Luyu Wang, Guangyao Zhou, and Fabio Viola. The DeepMind JAX Ecosystem, 2020. URL <http://github.com/google-deeppmind>.
- Yalchin Efendiev and Thomas Y Hou. *Multiscale finite element methods: theory and applications*, volume 4. Springer Science & Business Media, 2009.
- Yalchin Efendiev, Juan Galvis, and Xiao-Hui Wu. Multiscale finite element methods for high-contrast problems using local spectral basis functions. *Journal of Computational Physics*, 230(4):937–955, 2011.
- Yalchin Efendiev, Juan Galvis, and Thomas Y Hou. Generalized multiscale finite element methods (gmsfem). *Journal of computational physics*, 251:116–135, 2013.
- Vladimir Sergeevich Fanaskov and Ivan V Oseledets. Spectral neural operators. In *Doklady Mathematics*, volume 108, pp. S226–S232. Springer, 2023.
- Matthew W Farthing and Fred L Ogden. Numerical solution of richards’ equation: A review of advances and challenges. *Soil Science Society of America Journal*, 81(6):1257–1269, 2017.
- Nicola Rares Franco, Andrea Manzoni, Paolo Zunino, and Jan S Hesthaven. Deep orthogonal decomposition: a continuously adaptive neural network approach to model order reduction of parametrized partial differential equations.
- Zhongkai Hao, Zhengyi Wang, Hang Su, Chengyang Ying, Yinpeng Dong, Songming Liu, Ze Cheng, Jian Song, and Jun Zhu. Gnot: A general neural operator transformer for operator learning. In *International Conference on Machine Learning*, pp. 12556–12569. PMLR, 2023.
- Roland Haverkamp, Michel Vauclin, Jaoudat Touma, PJ Wierenga, and Georges Vachaud. A comparison of numerical simulation models for one-dimensional infiltration. *Soil Science Society of America Journal*, 41(2):285–294, 1977.

- Jan S Hesthaven and Stefano Ubbiali. Non-intrusive reduced order modeling of nonlinear problems using neural networks. *Journal of Computational Physics*, 363:55–78, 2018.
- George Em Karniadakis, Ioannis G Kevrekidis, Lu Lu, Paris Perdikaris, Sifan Wang, and Liu Yang. Physics-informed machine learning. *Nature Reviews Physics*, 3(6):422–440, 2021.
- Patrick Kidger and Cristian Garcia. Equinox: neural networks in JAX via callable PyTrees and filtered transformations. *Differentiable Programming workshop at Neural Information Processing Systems 2021*, 2021.
- Nikola Kovachki, Zongyi Li, Burigede Liu, Kamyar Azizzadenesheli, Kaushik Bhattacharya, Andrew Stuart, and Anima Anandkumar. Neural operator: Learning maps between function spaces with applications to pdes. *Journal of Machine Learning Research*, 24(89):1–97, 2023.
- Fabian Kröpfel, Roland Maier, and Daniel Peterseim. Operator compression with deep neural networks. *Advances in Continuous and Discrete Models*, 2022(1):29, 2022.
- Fabian Kröpfel, Daniel Peterseim, and Elisabeth Ullmann. Neural network localized orthogonal decomposition for numerical homogenization of diffusion operators with random coefficients. *arXiv preprint arXiv:2509.12896*, 2025.
- Zongyi Li, Nikola Kovachki, Kamyar Azizzadenesheli, Burigede Liu, Kaushik Bhattacharya, Andrew Stuart, and Anima Anandkumar. Fourier neural operator for parametric partial differential equations. *arXiv preprint arXiv:2010.08895*, 2020.
- Burigede Liu, Eric Ocegueda, Margaret Trautner, Andrew M Stuart, and Kaushik Bhattacharya. Learning macroscopic internal variables and history dependence from microscopic models. *Journal of the Mechanics and Physics of Solids*, 178:105329, 2023.
- Ilya Loshchilov and Frank Hutter. Decoupled weight decay regularization. *arXiv preprint arXiv:1711.05101*, 2017.
- Lu Lu, Pengzhan Jin, and George Em Karniadakis. Deeponet: Learning nonlinear operators for identifying differential equations based on the universal approximation theorem of operators. *arXiv preprint arXiv:1910.03193*, 2019.
- Lu Lu, Pengzhan Jin, Guofei Pang, Zhongqiang Zhang, and George Em Karniadakis. Learning nonlinear operators via deeponet based on the universal approximation theorem of operators. *Nature machine intelligence*, 3(3):218–229, 2021.
- Huakun Luo, Haixu Wu, Hang Zhou, Lanxiang Xing, Yichen Di, Jianmin Wang, and Mingsheng Long. Transolver++: An accurate neural solver for pdes on million-scale geometries. *arXiv preprint arXiv:2502.02414*, 2025.
- André LG Mandolesi. Asymmetric geometry of total grassmannians. *arXiv preprint arXiv:2310.17865*, 2023.
- Brek Meuris, Saad Qadeer, and Panos Stinis. Machine-learning custom-made basis functions for partial differential equations. *arXiv preprint arXiv:2111.05307*, 2021.
- Brek Meuris, Saad Qadeer, and Panos Stinis. Machine-learning-based spectral methods for partial differential equations. *Scientific Reports*, 13(1):1739, 2023.
- Lorenzo Adolph Richards. Capillary conduction of liquids through porous mediums. *physics*, 1(5): 318–333, 1931.
- Denis Spiridonov, Sergei Stepanov, and Tina Mai. Prediction of discretization of online gmsfem using deep learning for richards equation. *Journal of Computational and Applied Mathematics*, 454:116167, 2025.
- Theofanis Strouboulis, Ivo Babuška, and Kevin Copps. The design and analysis of the generalized finite element method. *Computer methods in applied mechanics and engineering*, 181(1-3):43–69, 2000.

Alasdair Tran, Alexander Mathews, Lexing Xie, and Cheng Soon Ong. Factorized fourier neural operators. *arXiv preprint arXiv:2111.13802*, 2021.

Maria Vasilyeva, Wing T Leung, Eric T Chung, Yalchin Efendiev, and Mary Wheeler. Learning macroscopic parameters in nonlinear multiscale simulations using nonlocal multicontinua upscaling techniques. *Journal of Computational Physics*, 412:109323, 2020.

Maria Vasilyeva, Aleksei Tyrylgin, Donald L Brown, and Anirban Mondal. Preconditioning markov chain monte carlo method for geomechanical subsidence using multiscale method and machine learning technique. *Journal of Computational and Applied Mathematics*, 392:113420, 2021.

Stefan Volkwein. Proper orthogonal decomposition: Theory and reduced-order modelling. *Lecture Notes, University of Konstanz*, 4(4):1–29, 2013.

Min Wang, Siu Wun Cheung, Wing Tat Leung, Eric T Chung, Yalchin Efendiev, and Mary Wheeler. Reduced-order deep learning for flow dynamics. the interplay between deep learning and model reduction. *Journal of Computational Physics*, 401:108939, 2020.

Sifan Wang, Hanwen Wang, and Paris Perdikaris. Learning the solution operator of parametric partial differential equations with physics-informed deepnets. *Science advances*, 7(40):eabi8605, 2021.

Eugene Wong. Stochastic processes in information and dynamical systems. (*No Title*), 1971.

A COARSE GRID

The notation ω_i refers to the i -th local domain, where the index corresponds to the numbering of points on the coarse grid. Fig. 2 shows examples of local domains ω_0 , ω_{20} , and ω_{34} , representing the **full**, **half**, and **corner** types in 2D. In 3D, there are four types: **full** (8 cells), **half** (4 cells), **quarter** (2 cells), and **corner** (1 cell), where the cell is a cube. Each local domain is discretized with a fine grid.

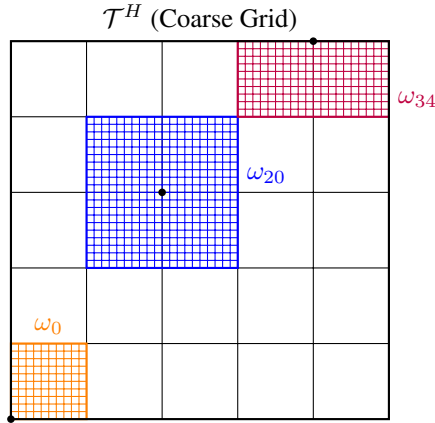


Figure 2: Illustration of a 5×5 coarse grid \mathcal{T}_H showing local domains of different types: the **corner** type ω_0 (1 cell), **half** type ω_{34} (2 cells), and **full** type ω_{20} (4 cells), where the cell is a square.

B TRAINING GMSFEM-NO

We train separate specialized NOs for each geometric domain type: three for 2D problems (full, half, corner) and four for 3D problems (full, half, quarter, corner), as illustrated for the 2D case in Fig. 3 (a-c). Each NO predicts the N_{bf} basis functions for all local domains of its assigned type.

The number of local domains for each geometric type can be calculated based on the coarse grid dimensions. For a 2D grid with 36 domains (5×5 cells), the counts are: 16 full, 16 half, and 4 corner

domains. For a finer 2D grid with 121 domains (10×10 cells), the counts are: 81 full, 36 half, and 4 corner domains. In 3D, for a grid with 216 domains ($5 \times 5 \times 5$ cells), the distribution is: 64 full, 96 half, 48 quarter, and 8 corner domains. In 3D, for a finer grid with 729 domains ($8 \times 8 \times 8$ cells), the distribution is: 343 full, 294 half, 84 quarter, and 8 corner domains.

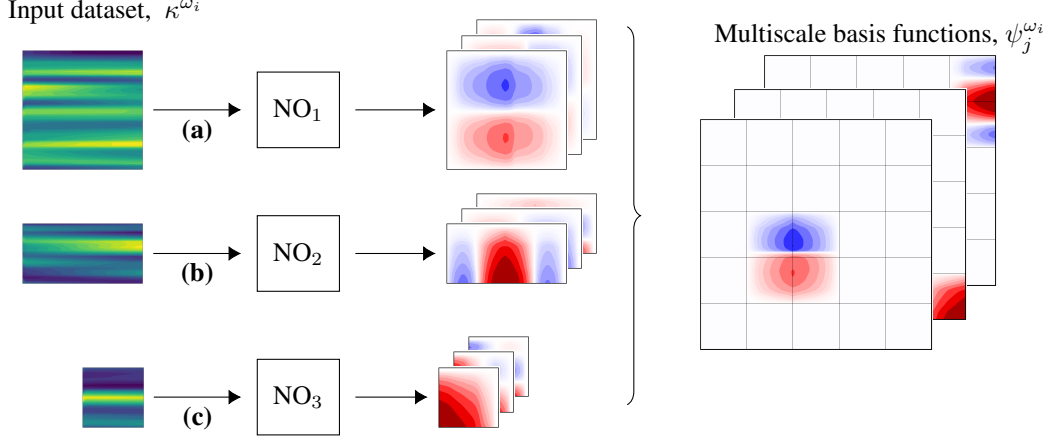


Figure 3: Multiscale basis generation algorithm for three subdomain types ω_i : **(a) full**, **(b) half**, **(c) corner** - using dedicated NOs per type with further extension to Ω .

C SUBSPACE ALIGNMENT LOSS (SAL)

To understand the relationship between the proposed \mathcal{L}_{SAL} (5) and classical Grassmannian geometry Bendokat et al. (2024); Mandolesi (2023), we begin with the orthogonal projection matrices. For a subspace R spanned by a set of basis vectors, we compute an orthonormal basis Q_R via the thin QR decomposition. The orthogonal projection matrix onto R is then given by $P_R = Q_R Q_R^\top$.

The Grassmannian distance between two k -dimensional subspaces R and \tilde{R} is defined using these projection matrices. The distance derivation proceeds as follows:

$$\begin{aligned} \|P_R - P_{\tilde{R}}\|_F^2 &= \text{tr}(P_R) - 2\text{tr}(P_R P_{\tilde{R}}) + \text{tr}(P_{\tilde{R}}) = \dim(R) + \dim(\tilde{R}) - 2\text{tr}(P_R P_{\tilde{R}}) \\ &= 2\left(k - \text{tr}(Q_R Q_R^\top Q_{\tilde{R}} Q_{\tilde{R}}^\top)\right). \end{aligned}$$

The matrix $Q_R^\top Q_{\tilde{R}}$ contains the cosines of the principal angles between the subspaces. Therefore,

$$\|P_R - P_{\tilde{R}}\|_F^2 = 2\left(k - \|Q_R^\top Q_{\tilde{R}}\|_F^2\right).$$

Consequently, the Grassmannian distance simplifies to:

$$d(R, \tilde{R}) = \frac{1}{\sqrt{2}} \|P_R - P_{\tilde{R}}\|_F = \sqrt{k - \|Q_R^\top Q_{\tilde{R}}\|_F^2}.$$

This derivation confirms that minimizing \mathcal{L}_{SAL} is equivalent to minimizing the expected Grassmannian distance between the true and predicted subspaces.

In considering the theoretical soundness of our approach, we note that a formal upper bound linking principal angles to the final error would further strengthen the framework. When the SAL loss is small, it ensures that the learned solution remains close to the exact solution. To formalize this, let Q_{R^c} represent the multiscale solution computed using GMsFEM and $Q_{\tilde{R}^c}$ denote the learned

solution. The error can then be bounded as follows:

$$\begin{aligned} \|u - Q_{\tilde{R}}c\|^2 &\leq \|u - Q_Rc\|^2 + \|Q_Rc - Q_{\tilde{R}}c\|^2 = \\ &\|u - Q_Rc\|^2 + c^\top (Q_R - Q_{\tilde{R}})^\top (Q_R - Q_{\tilde{R}})c = \\ &\|u - Q_Rc\|^2 + 2c^\top (I - (Q_R)^\top Q_{\tilde{R}})c. \end{aligned} \quad (10)$$

The first term is GMsFEM error (which is small), and the second term is small if $I - (Q_R)^\top Q_{\tilde{R}}$ is small. The norm above can play an important role in the proof. Since the GMsFEM error is done in energy norm, in general, one needs to take the energy norm, which is non-local and can slow down computations.

This error estimate gives a bound between the learned solution and the angle between the spaces. To estimate the angle via the solution error is more difficult. Indeed, these questions need to be addressed in the future and will help to choose the appropriate loss functions.

D $\mathcal{L}_{\text{SAL-PR}}$

The primary role of \mathcal{L}_{SAL} (5) is to enforce geometric alignment between the learned subspace \tilde{R}^i and the target GMsFEM subspace R^i . However, this loss has a specific limitation: it is invariant to rotations within the subspace. If $Q_{\tilde{R}^i} = Q_{R^i}U$ for any unitary matrix U (s.t. $U^\top U = I$), the subspaces are considered identical under this metric, as:

$$N_{\text{bf}} - \|Q_{R^i}^\top Q_{\tilde{R}^i}\|_F^2 = N_{\text{bf}} - \|U\|_F^2 = 0$$

This geometric alignment may overlook finer discrepancies in how specific functions are projected. The $\mathcal{L}_{\text{SAL-PR}}$ (6) term was introduced to address this theoretical gap by directly enforcing projection consistency. It tests the subspaces with random vectors v^i drawn from the target subspace R^i . Since v^i lies in R^i , its projection via the true basis is itself: $P_{R^i}v^i = v^i$. The discrepancy $(I - P_{\tilde{R}^i})v^i$ thus represents the projection error. Minimizing this forces the learned subspace to correctly capture arbitrary vectors from the target subspace, going beyond mere geometric overlap.

E THE SIGN INVARIANCE OF BASIS FUNCTIONS

Multiscale basis functions $\psi_j^{\omega_i}$ are derived from local eigenvectors $\phi_j^{\omega_i}$ via $\psi_j^{\omega_i} = \chi_i \phi_j^{\omega_i}$, where χ_i is a partition of unity function and $\phi_j^{\omega_i}$ solve the symmetric generalized eigenvalue problem:

$$A_h^{\omega_i} \phi = \lambda S_h^{\omega_i} \phi,$$

where $A_h^{\omega_i}$ and $S_h^{\omega_i}$ are symmetric matrices. These eigenvectors satisfy the orthogonality relations:

$$\phi_j^\top A_h^{\omega_i} \phi_k = \lambda_j \delta_{jk}, \quad \phi_j^\top S_h^{\omega_i} \phi_k = \delta_{jk}.$$

Since eigenvectors are defined only up to a scalar multiple, if ϕ_j is an eigenvector corresponding to eigenvalue λ_j , then $-\phi_j$ is also a valid eigenvector for the same eigenvalue. Both choices satisfy the orthogonality and normalization conditions above, meaning the sign of each basis function is arbitrary and does not affect its mathematical properties.

To address this sign ambiguity, we define the RBFL₂ loss as:

$$\mathcal{L}_{\text{RBFL}_2} = \mathbb{E}_{i,j} \left[\min \left(\frac{\|\psi_j^i - \tilde{\psi}_j^i\|_2^2}{\|\psi_j^i\|_2^2}, \frac{\|\psi_j^i + \tilde{\psi}_j^i\|_2^2}{\|\psi_j^i\|_2^2} \right) \right],$$

where ψ_j^i are the final multiscale basis functions (typically obtained by multiplying eigenvectors by partition of unity functions). This loss compares the prediction $\tilde{\psi}_j^i$ against both ψ_j^i and $-\psi_j^i$, selecting the smaller error to account for the sign invariance.

F INPUT DATA

We use the Karhunen-Loève expansion (KLE) Wong (1971); Aarnes & Efendiev (2008); Vasilyeva et al. (2021) to generate stochastic permeability fields. This method decomposes a random field into deterministic spatial functions and random coefficients.

1. Covariance Function. We assume the covariance function has an exponential form:

$$R(x, y) = \sigma_R^2 \exp(-\sqrt{\Delta^2}),$$

with

$$\Delta^2 = \frac{|x_1 - x_2|^2}{l_x^2} + \frac{|y_1 - y_2|^2}{l_y^2},$$

for 2D case and

$$\Delta^2 = \frac{|x_1 - x_2|^2}{l_x^2} + \frac{|y_1 - y_2|^2}{l_y^2} + \frac{|z_1 - z_2|^2}{l_z^2},$$

for 3D case with correlation lengths l_x, l_y, l_z and variance σ_R^2 :

- For the 2D case: $l_x = 0.02$, $l_y = 0.6$, $\sigma_R^2 = 2$;
- For the 3D case: $l_x = 0.02$, $l_y = 0.6$, $l_z = 0.2$, $\sigma_R^2 = 2$.

2. Eigenvalue Problem. The eigenfunctions ϕ_k and eigenvalues λ_k are obtained by solving the homogeneous Fredholm integral equation:

$$\int_{\Omega} R(x, y) \phi_k(y) dy = \lambda_k \phi_k(x), \quad k = 1, 2, \dots,$$

3. Random Field Construction. The random field is represented as:

$$Y_L(x, \omega) = \sum_{k=1}^L \sqrt{\lambda_k} \theta_k(\omega) \phi_k(x),$$

where $\theta_k(\omega)$ are scalar random variables, and L is chosen to capture most of the field's energy by retaining the largest eigenvalues.

4. Permeability Field Generation. Each stochastic permeability field is defined as:

$$\kappa(x, \omega) = \exp(a_k \cdot \phi(x, \omega)),$$

where $\phi(x, \omega)$ represents the heterogeneous porosity field derived from $Y_L(x, \omega)$, and $a_k > 0$ is a scaling parameter that controls the contrast.

This KLE framework provides a systematic approach for generating realistic permeability fields with prescribed spatial correlation structures. An example of a 2D input coefficient field $\kappa(x)$ is shown in Fig. 4.

The **spatially variable forcing term** is defined by

$$f(x) \sim \gamma \cdot \mathcal{N}\left(\alpha \cdot (I - \Delta)^{-\beta}\right),$$

where \mathcal{N} denotes a Gaussian random field. The parameters are set as follows:

- For the 2D case: $\gamma = 2000$, $\alpha = 1$, and $\beta = 0.5$;
- For the 3D case: $\gamma = 2000$, $\alpha = 2$, and $\beta = 1$.

An example of a 2D right-hand side $f(x)$ is shown in Fig. 4.

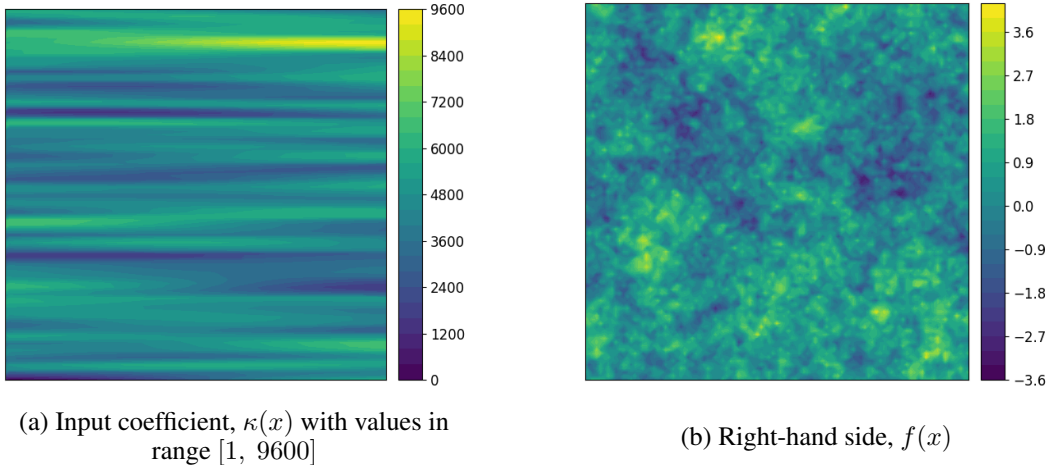


Figure 4: Example of input coefficient and right-hand side.

G BASELINES VS. GMSFEM-NO

We compare GMSFEM-NO with several baselines:

1. **POD** Volkwein (2013). Classical global intrusive POD.
2. **Intrusive POD with DeepONet/FFNO or POD basis** Meuris et al. (2021), Meuris et al. (2023). First selected neural network is trained on standard regression problem. After that one extract basis from trained network and uses similar to intrusive POD to form reduced model. For **FFNO** Tran et al. (2021) basis is extracted from the last hidden layer, for **DeepONet** Lu et al. (2019) basis is extracted from trunk net.
3. **PCA-Net** Hesthaven & Ubbiali (2018), Bhattacharya et al. (2021). POD is used to compress features and targets, MLP is used as processor.
4. **Kernel** Batlle et al. (2024). Vector RKHS method is used to map sampled input functions to sampled output functions.
5. **DeepPOD** Franco et al.. A DL-based techniques used to directly learn optimal basis with projector-based loss.

We use dataset with spatially variable forcing term (9) covered in more details in Appendix F. Neural networks was trained and evaluated on grid 100×100 .

For each selected baseline we perform sweep over hyperparameters:

1. **Intrusive POD with FFNO basis.** Architecture is defined by the number of features in the hidden layer, number of modes used by spectral convolution, and number of layers. Number of features in the hidden layer was fixed to 64, number of modes was selected from the set $[10, 14, 16]$, number of layers – from the set $[3, 4, 5]$. Optimisation was performed with Lion optimiser Chen et al. (2023) with exponential decay 0.5 with number of transition steps selected from $[100, 200]$, and learning rate selected from $[5 \cdot 10^{-5}, 10^{-4}]$. We optimise for 1000 epoch with batch size 10. In all architectures we used GELU activation function.
2. **Intrusive POD with DeepONet basis.** Architecture is defined by trunk and branch nets. As trunk net we used convolution architecture with spatial downsampling by a factor of 2 along each dimension after each layer, simultaneously, the number of channels was multiplied by 2 after each layer, as branch net we used standard MLP. We apply optimisation similar to the one of FFNO, but select learning rate from $[10^{-3}, 10^{-4}]$. Number of trunk network layers was fixed to 4, trunk encoder transformed 2 input features to either 4 or 5 features, kernel size of convolution in trunk was selected among $[3, 7]$. In the branch net we vary number of layers $[3, 4]$ and the number of basis vectors $[100, 200]$ in the last layer.
3. **DeepPOD** Grid search for DeepPOD was exactly the same as for Intrusive POD with FFNO.

4. **PCANet.** For PCANet the optimisation was similar to Intrusive POD with DeepONet, but with 3000 epochs. We vary the sizes of POD encoder and decoder among [100, 300, 500] and [100, 300, 500]. For MLP processor we vary the number of layers [3, 4, 5] and the number of hidden neurons [100, 300, 500].
5. **Kernel.** We closely followed code provided by authors. As kernels we used Matern, RBF. We combined the method with POD and performed a grid search over the number of modes: [50, 100, 150, 200] for both features and targets.

Table 10: Regression-based methods.

method	train error	test error
GMsFEM-NO	2.6%	2.8%
PCANet	6%	24%
kernel	7%	100%

Comparison of regression-based approaches with GMsFEM-NO appears in Table 10. We observe significant overfitting for kernel-based method and PCA-Net.

Intrusive techniques are compared in Figure 5. We see that bases extracted from DeepONet and FFNO are generally not appealing. FFNO slightly improves over global POD (weak baseline) for $\simeq 64$ basis functions. DeepONet fails to reach accuracy of global POD. The most competitive approach is DeepPOD. Note however, that DeepPOD becomes comparable to GMsFEM-NO with 8 sparse (localised) basis functions only when it uses 20 dense basis functions. With 30 basis functions DeepPOD outperforms GMsFEM-NO with 8 basis functions.

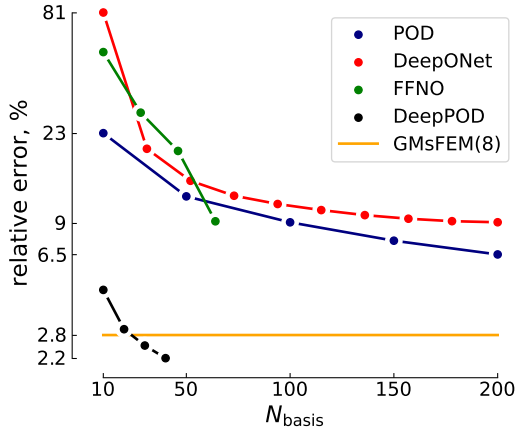


Figure 5: Comparison of accuracy for intrusive techniques. Number of basis functions for GMsFEM is fixed to 8. DeepONet and FFNO mean Intrusive POD with DeepONet/FFNO basis.

H GMSFEM-NO TRAINING DETAILS

For F-FNO training to predict basis functions subspace, we used AdamW optimizer Loshchilov & Hutter (2017) with cosine decay learning rate scheduler. The initial learning rate was $1 \cdot 10^{-3}$. We trained NO for 600 epochs. The best number of random test vectors v^i is 10 (see the Table 11). For the rest of the hyperparameters, we performed a grid search:

1. Batch size [8, 16, 32].
2. Number of operator layers [4, 5].
3. Number of modes used in F-FNO kernel:
 - For 2D:

- for full domains $[[16, 16], [18, 18]]$;
- for half domains $[[8, 8], [10, 10], [14, 8], [14, 10]]$;
- for corner domains $[[6, 6], [8, 8], [10, 10]]$.
- For 3D:
 - for full domains $[[6, 6, 6], [8, 8, 8]]$;
 - for half domains $[[8, 8, 4], [6, 6, 3]]$;
 - for quarter domains $[[8, 4, 4], [6, 3, 3]]$.
 - for corner domains $[[4, 4, 4], [3, 3, 3]]$.
- 4. Number of channels in the FFNO kernel $[64, 128]$.

Table 11: Performance GMsFEM-NO for 2D (100×100 , $N_v = 36$).

Dataset	GMsFEM-NO, $\mathcal{L}_{\text{SAL-PR}}$							
	$v^i = 5$		$v^i = 10$		$v^i = 15$		$v^i = 20$	
	L_2	H_1	L_2	H_1	L_2	H_1	L_2	H_1
Diffusion, 8	1.09%	11.90%	1.06%	11.65%	1.31%	12.34%	1.10%	12.13%
Diffusion, 9	2.84%	19.14%	2.81%	19.03%	2.88%	19.38%	2.87%	19.37%
Richards, 8	1.91%	11.21%	1.87%	11.25%	1.98%	11.75%	1.94%	11.64%
Richards, 9	2.91%	20.06%	2.99%	19.60%	2.96%	20.33%	2.94%	20.26%

The source code containing the optimal parameters will be made publicly available upon acceptance. We use JAX, Optax DeepMind et al. (2020) and Equinox Kidger & Garcia (2021) in all experiments.

I F-FNO, GNOT, TRANSOLVER++ TRAINING DETAILS

I.1 F-FNO TRAINING DETAILS

For F-FNO Tran et al. (2021), we used the following training protocol. We employed the AdamW optimizer Loshchilov & Hutter (2017) with a cosine decay learning rate scheduler and trained for 600 epochs, using a base learning rate of 10^{-3} . We performed a grid search over the following hyperparameters:

1. Batch size: $[8, 16, 32]$;
2. Number of modes in F-FNO kernel: $[14, 16]$;
3. Number of operator layers: $[4, 5]$;
4. Number of channels in F-FNO kernel: $[64, 128]$.

The optimal hyperparameters were: batch size 8, 5 operator layers, 16 modes, and 128 channels.

I.2 GNOT TRAINING DETAILS

For GNOT Hao et al. (2023), we employed the following training protocol: AdamW optimizer with a onecycle learning rate scheduler for 600 epochs, using a base learning rate of 10^{-3} . We conducted a grid search over hyperparameters that were previously found optimal for different 2D problems in Hao et al. (2023):

1. Batch size: $[4, 8]$
2. Number of attention layers: $[3, 4]$
3. Hidden size of attention and input embeddings: $[96, 128, 192]$
4. Number of MLP layers: $[3, 4]$

5. Hidden size of MLP: [128, 192]
6. Number of heads: [4, 8]
7. Number of experts: [3, 4]

The optimal configuration was: batch size 4, 4 attention layers, hidden size of 128 for attention, MLP, and input embeddings, 8 heads, 4 experts, and 4 MLP layers.

I.3 TRANSOLVER++ TRAINING DETAILS

For Transolver++ Luo et al. (2025), we employed the following training protocol: AdamW optimizer with a onecycle learning rate scheduler for 600 epochs, using a base learning rate of 10^{-3} . We conducted a grid search over hyperparameters previously identified as optimal for 2D problems in Luo et al. (2025):

1. Batch size: [4, 8]
2. Number of layers: [4, 8]
3. Hidden size: [128, 256]
4. Number of MLP layers: [1, 2]
5. Number of heads: [4, 8]
6. Slices: [32, 64]

The optimal configuration was: batch size 4, 8 layers, hidden size 256, 2 MLP layers, 8 heads, and 64 slices.

J RESULTS OF GMSFEM-NO FOR $N_{\text{BF}} = 4$

Table 12: Performance comparison of loss functions for NO training (100×100 grid, $N_v = 36$).

N_{bf}	Dataset	$\mathcal{L}_{\text{RBFL}_2}$		\mathcal{L}_{SAL}		$\mathcal{L}_{\text{SAL-PR}}$	
		L_2	H_1	L_2	H_1	L_2	H_1
4	Diffusion, 8	2.72%	19.10%	2.39%	18.01%	2.40%	18.01%
	Diffusion, 9	6.03%	29.10%	5.76%	28.40%	5.78%	28.43%
	Richards, 8	3.87%	16.26%	3.14%	15.01%	3.17%	15.02%
	Richards, 9	9.78%	34.39%	6.11%	29.37%	6.13%	29.42%

For the Richards equation with complex right-hand side (9) and $N_{\text{bf}} = 4$ basis functions, our proposed loss improves the relative L_2 metric by a factor of 1.6.

We did not conduct further experiments with GMSFEM-NO using $N_{\text{bf}} = 4$ because its performance was insufficient and it underperformed compared to the standalone neural operator.

K OUT-OF-DISTRIBUTION RESULTS

Unlike standalone NOs, which suffer from catastrophic failure when applied to out-of-distribution forcing terms (Table 13), GMSFEM-NO is fundamentally independent of the right-hand side, ensuring robust performance. Retraining the NO for new right-hand side terms requires computationally expensive recalculation of solutions, highlighting a key limitation of standalone NO learning.

Table 13: Out-of-distribution results for the NO: training and testing on PDEs with different right-hand sides.

Train, $\mathcal{D}_{\text{train}}$	Test, $\mathcal{D}_{\text{test}}$	100×100	250×250
Diffusion, 8	Diffusion, 9	218%	174%
Diffusion, 9	Diffusion, 8	1392%	1632%
Richards, 8	Richards, 9	196%	113%
Richards, 9	Richards, 8	6503%	6554%

L HEAT EQUATION FOR 2D

We consider the heat equation with heterogeneous coefficient

$$\begin{aligned} \frac{\partial u}{\partial t} - \nabla \cdot (\kappa(x) \nabla u(x)) &= f(x), \quad x \in \Omega \times (0, T_{\max}], \\ u &= 0, \quad x \in \partial\Omega \times (0, T_{\max}], \\ u|_{t=0} &= 0, \quad x \in \Omega, \end{aligned}$$

where time parameters: $\Delta t = 2.5 \cdot 10^{-6}$, $T_{\max} = 5 \cdot 10^{-4}$. We consider two right-hand side configurations:

- Uniform unit forcing term

$$f(x) = 1; \tag{11}$$

- Spatially variable forcing defined by

$$f(x) = \sin(\pi x) \cos(\pi y). \tag{12}$$

Table 14: Performance comparison of GMsFEM and GMsFEM-NO for Heat equation for 2D (250×250 , $N_v = 121$).

N_{bf}	Dataset	GMsFEM		GMsFEM-NO, \mathcal{L}_{SAL}	
		L_2	H_1	L_2	H_1
8	Heat, 11	0.72%	10.81%	0.78%	13.06%
	Heat, 12	1.13%	19.92%	1.17%	21.57%

The results, presented in the Table 14, show that our proposed GMsFEM-NO method with \mathcal{L}_{SAL} maintains high accuracy for this time-dependent problem, with relative L_2 errors below 1.2%. This demonstrates the successful application of our framework to time-dependent problems.

M DIFFUSION EQUATION WITH MIXED BOUNDARY CONDITIONS

We consider the diffusion equation with heterogeneous coefficient

$$\begin{aligned} -\nabla \cdot (\kappa(x) \nabla u(x)) &= f(x), \quad x \in \Omega \equiv (0, 1)^2, \\ u &= 0, \quad x \in \Gamma_D, \\ \kappa(x) \frac{\partial u}{\partial n} &= \alpha \cdot (u - u_{\text{const}}), \quad x \in \Gamma_R, \end{aligned}$$

where the boundary is partitioned into a Dirichlet part $\Gamma_D = \{x \in \partial\Omega \mid y = 0\}$ and a Robin part $\Gamma_R = \{x \in \partial\Omega \mid y = 1\}$ with parameters: Robin coefficient $\alpha = 1$, $u_{\text{const}} = 1$.

Our framework demonstrates robust performance when extended to problems with mixed boundary conditions, maintaining high accuracy even in these more complex scenarios. As shown in Table 15, the GMsFEM-NO method with \mathcal{L}_{SAL} achieves relative L_2 errors of approximately 1.2% for diffusion problems with Robin boundary conditions. This represents a significant extension beyond the homogeneous Dirichlet conditions typically considered in multiscale methods.

Table 15: Performance comparison of GMsFEM and GMsFEM-NO for equation with mixed boundary conditions for 2D (250×250 , $N_v = 121$).

N_{bf}	Dataset	GMsFEM		GMsFEM-NO, \mathcal{L}_{SAL}	
		L_2	H_1	L_2	H_1
8	Diffusion, 8	1.11%	7.98%	1.22%	12.10%
	Diffusion, 9	1.09%	7.72%	1.23%	12.31%

N TIME

The core objective of GMsFEM-NO is to reduce the cost of the traditional GMsFEM offline stage over many subsequent simulations. To provide full transparency, we have performed a detailed analysis that compares two practical scenarios: training models sequentially (one after another on one GPU) and in parallel. The breakeven point x is the number of inference samples where the total time of GMsFEM-NO (including training data generation and training) equals that of using standard GMsFEM for all samples:

$$T_{\text{data}} + T_{\text{train}} + T_{\text{inf}} \cdot x = T_{\text{GMsFEM}} \cdot x,$$

where T_{data} is the wall-clock time for generating training data via traditional GMsFEM, T_{train} is the total wall-clock time for training NO (which varies by scenario), T_{GMsFEM} is the wall-clock time for a single offline GMsFEM basis generation, and T_{inf} is the wall-clock time for a single GMsFEM-NO inference. The results are in the Table 16.

Even with sequential training, the method pays off for multi-query scenarios. The benefit is larger for large-scale 3D problems, where the breakeven point remains low (159 samples) due to the high cost of the traditional GMsFEM solver.

Table 16: Performance comparison of sequential and parallel implementations

Problem Configuration	Performance Metrics					
	T_{GMsFEM}	T_{inf}	Samples	Implementation	T_{train}	x
100×100	16.87	0.28	800	Sequential	37800	-3270
	16.87	0.28	800	Parallel	12600	-1570
250×250	210.5	0.31	800	Sequential	43200	-1040
	210.5	0.31	800	Parallel	14400	-870
$50 \times 50 \times 50$	935.4	0.84	800	Sequential	86400	-1090
	935.4	0.84	800	Parallel	21600	-820
$100 \times 100 \times 100$	10547.2	1.33	150	Sequential	100800	-159
	10547.2	1.33	150	Parallel	25200	-152